

Frontogenesis of the Angola-Benguela Frontal Zone

Shunya Koseki¹, Hervé Giordani², and Katerina Goubanova^{3,4},

1. Geophysical Institute, University of Bergen, Bergen/Bjerknes Centre for Climate Research, Norway
2. Centre National de Recherches Météorologiques, MÉTÉO-France, Toulouse, France
3. Centro de Estudios Avanzados en Zonas Áridas, La Serena, Chile
4. CECI/CERFACS-CNRS, Toulouse, France

Correspondence to Shunya Koseki

Email: Shunya.Koseki@gfi.uib.no

Address: Geophysical Institute, University of Bergen, Postboks 7803, 5020, Bergen, Norway

1 **Abstract**

2 A diagnostic analysis of the climatological annual mean and seasonal cycle of the
3 Angola Benguela Frontal Zone (ABFZ) is performed applying an ocean frontogenesis
4 function (OFGF) to the ocean mixing layer (OML). The OFGF reveals that
5 meridional confluence and the vertical tilting terms are the most dominant
6 contributors to the frontogenesis of the ABFZ. The ABFZ shows a well-pronounced
7 semi-annual cycle with two maximum (minimum) peaks in April-May and
8 November-December (February-March and July-August). The development of the
9 two maxima of frontogenesis is due to two different physical processes: enhanced
10 tilting from March to April and the meridional confluence from September to October.
11 The strong meridional confluence in September-October is closely related to the
12 seasonal southward intrusion of tropical warm water to the ABFZ that seems to be
13 associated with the development of the Angola Dome northwestern of the ABFZ. The
14 strong tilting effect from March to April is attributed to the meridional gradient of
15 vertical velocities whose effect is amplified in this period due to increasing
16 stratification and shallow OML depth. The proposed OFGF can be viewed as a tool to
17 diagnose the performance of Coupled General Circulation Models (CGCMs) that
18 generally fail in simulating realistically the position of the ABFZ, which leads to huge
19 warm biases in the southeastern Atlantic.

20

21

22

23

24

25 **1. Introduction**

26 The Angola-Benguela Frontal Zone (ABFZ, see Fig. 1), situated off the coast
27 of Angola/Namibia, is a key oceanic feature in the southeastern Atlantic Ocean. The
28 ABFZ separates the warm sea water of the Angola Current (e.g., Kopte et al., 2017)
29 from the cold sea water associated with the Benguela Current/upwelling system (e.g.,
30 Mohrholz et al., 2004; Colberg and Reason, 2006; Veitch et al., 2006; Colberg and
31 Reason, 2007; Fennel et al., 2012; Goubanova et al., 2013; Junker et al., 2015; Junker
32 et al., 2017; Vizzy et al., 2018). The ABFZ is characterized by smaller spatial extent
33 and weaker SST gradient compared to the major oceanic fronts generated by the
34 western boundary currents (Fig. 1). However, due to its near coastal location, the
35 ABFZ plays important roles for the southern African continent, strongly impacting
36 local marine ecosystem (e.g., Auel and Verheye, 2007; Chavez and Messié, 2009) and
37 regional climate (Hirst and Hastenrath, 1983; Rouault et al. 2003; Hansingo and
38 Reason, 2009; Manhique et al., 2015). In particular, the main mode of interannual
39 variability of SST in the ABFZ, so-called Benguela Niño/Niña (e.g., Florenchie et al.,
40 2003; Rouault et al., 2017), influences the local rainfall along the southwestern
41 African coast of Angola and Namibia [via moisture flux anomalies associated with the](#)
42 [SST anomalies](#) (Rouault et al., 2003; Lutz et al., 2015) and tends to have a remote
43 impact on rainfall activity over the southeastern African continent (e.g., Manhique et
44 al., 2015).

45 The ABFZ region also poses one of the major challenges for the global climate
46 modeling community. Most CGCMs exhibit a huge warm SST bias in the ABFZ (e.g.,
47 Zuidema et al., 2016) and fail to reproduce the realistic SST, its seasonal cycle and the

48 right location of the ABFZ (e.g., Koseki et al., 2017). While Colberg and Reason
49 (2006) and Giordani et al. (2011) concluded that the position of the ABFZ is
50 controlled to a large extent by the local wind stress curl, Koseki et al. (2018)
51 elucidated that the local wind stress curl bias in GCMs contributes partly to the warm
52 SST bias in the ABFZ via erroneous intrusion of tropical warm water, which is
53 induced by the negative wind stress curl and enhanced Angola Current. In order to
54 [understand comprehensively the sources of such](#) model biases, one need to understand
55 the processes of generation of the ABFZ.

56 Previous studies have focused mainly on SST variability at seasonal and
57 interannual scales in the ABFZ and its impacts on regional climate are well-studied
58 (e.g., Rouault et al., 2003; Lutz et al., 2015). [Whereas Morholz et al. \(1999\) analyzed](#)
59 [the ABFZ during a particular event in 1999](#), to our knowledge, there are no works
60 quantitatively investigating dynamical and thermodynamical processes which
61 generate and maintain the ABFZ and its seasonal cycle. A dynamical diagnosis for the
62 SST front in the north of the Atlantic Cold Tongue (e.g., Hasternrath and Lamb, 1978;
63 Giordani et al., 2013) was proposed by Giordani and Caniaux (2014, hereafter
64 referred as GC2014). This frontogenetic function is, in general, adapted to explore
65 sources of frontogenesis of atmospheric synoptic-scale cyclones in the extratropics (e.
66 g., Keyser et al., 1988; Giordani and Caniaux, 2001). Using a frontogenetic function
67 GC2014 showed clearly that the convergence associated with the northern South
68 Equatorial Current and Guinea Current forces the SST-front intensity (frontogenetic
69 effect) and mixed-layer turbulent flux destroys the SST-front (frontolytic effect) in
70 climatology. Fundamentally, the frontogenetic function consists of three mechanical
71 terms (confluence, shear and tilting) and two thermodynamical terms (diabatic heating
72 and vertical mixing). Around the ABFZ, all these terms can be considered as

73 contributors to the frontogenesis due to: (1) the [confluence zone associated with the](#)
74 [southward](#) Angola and [northward](#) Benguela currents (confluence and shear). (2)
75 strong coastal upwelling (tilting) associated with Benguela current; (3) [radiation](#)
76 [budget modification due to](#) stratocumulus cloud deck (diabatic heating related to
77 radiation) associated with the cold SST and subsidence due to St. Helena Anticyclone
78 (e.g., Klein and Hartmann, 1993; Pfeifroth et al., 2012). So far, the relative roles of
79 these different processes in the frontogenesis of the ABFZ still need to be
80 investigated.

81 In this study, following the fundamental philosophy of GC2014, we attempt to
82 understand the mechanisms responsible for the [climatological](#) ABFZ development at
83 seasonal scale based on a first-order estimation. We propose an ocean frontogenetic
84 function in a different way from GC2014 (this study focuses on the ocean-mixed layer
85 mean front). The structure of the remainder of this paper is as follows: Section 2 gives
86 details of data set used in this study. In section 3, we derive the ocean frontogenetic
87 function. Section 4 provides a description of the climatological state around the
88 ABFZ. In section 5, we apply our diagnostic methodology to the ABFZ and
89 determine the main terms of the frontogenetic function controlling its annual cycle.
90 The associated processes are discussed in section 6. Finally we summarize and make
91 some concluding remarks in section 7.

92

93 **2. Data**

94 For an overview of SST and its meridional gradient in the ABFZ and
95 evaluation of reanalysis data, we employ the Optimum Interpolated Sea Surface
96 Temperature (OISST, Reynolds et al., 2002) released by National Oceanic and

97 Atmospheric Administration (NOAA) that has a quarter degree of horizontal
98 resolution and daily temporal resolution from 1982 to 2010. For the 3-dimensional
99 diagnostic analysis of the ABFZ, we utilize 1-hour forecast data of Climate Forecast
100 System Reanalysis (CFSR, Saha et al., 2010) developed by the National Centers for
101 Environmental Prediction (NCEP). The ocean component of this system is based on
102 MOM version 4p0d (Griffies et al., 2004) and implements data assimilation for the
103 forecast. This system provides 6-hourly data with a 0.5 degree horizontal resolution
104 and 70 vertical layers for ocean. This resolution is relatively coarse compared to
105 available regional ocean models in a forced mode with wind forcing from satellite
106 product. However, the advantage of a coupled ocean-atmosphere system CFSR is that
107 it allows avoiding spurious effects in wind forcing over coastal regions resulting from
108 the extrapolation in a 25-50km width coastal fringe where the wind cannot be
109 observed by scattermeters (Astudillo et al., 2017). Moreover, the wind satellite
110 products are generally available relatively short time period limiting investigation of
111 long-term climatology and seasonal cycle. In this paper we will analyze daily-means
112 (the procedure of data post-processing is given in Supplemental Information) and
113 utilize the CFSR outputs of velocity (horizontal and vertical), potential temperature,
114 net surface heat flux, ocean mixing layer depth, and sea surface height.

115

116 **3. Ocean Frontogenesis Function**

117 The ocean frontogenetic function (OFGF) is defined and applied to the ocean
118 mixing layer (OML) in order to propose a dynamical diagnosis of the
119 maintenance/generating process of the ABFZ. Following GC2014, we use the OFGF
120 as a tool to unravel the Lagrangian (pure) sources of the oceanic front. While there

121 are plentiful numbers of literature investigating the ocean front dynamics (e.g.,
 122 Dinniman and Rienecker, 1999), the concept of this OFGF has been hardly referred.
 123 The Lagrangian frontogenesis function, F , is defined as,

$$124 \quad F \equiv \frac{d}{dt} \left(\frac{\partial \theta}{\partial y} \right) \quad (3.1),$$

125 where, θ is the temperature. While the frontogenetic function is generally defined as
 126 the square of the horizontal gradient of the temperature (e.g., GC2014), our study
 127 employs only the meridional gradient of the temperature because the ABFZ SST-
 128 gradient is oriented South-North. The right hand side of Eq. 3.1 can be written as,

$$\begin{aligned} \frac{d}{dt} \left(\frac{\partial \theta}{\partial y} \right) &= u \frac{\partial}{\partial x} \left(\frac{\partial \theta}{\partial y} \right) + v \frac{\partial}{\partial y} \left(\frac{\partial \theta}{\partial y} \right) + w \frac{\partial}{\partial z} \left(\frac{\partial \theta}{\partial y} \right) + \frac{\partial}{\partial t} \left(\frac{\partial \theta}{\partial y} \right) \\ 129 \quad &= -\frac{\partial u}{\partial y} \frac{\partial \theta}{\partial x} - \frac{\partial v}{\partial y} \frac{\partial \theta}{\partial y} - \frac{\partial w}{\partial y} \frac{\partial \theta}{\partial z} + \frac{\partial}{\partial y} \left(\frac{\partial \theta}{\partial t} + u \frac{\partial \theta}{\partial x} + v \frac{\partial \theta}{\partial y} + w \frac{\partial \theta}{\partial z} \right) \\ &= -\frac{\partial u}{\partial y} \frac{\partial \theta}{\partial x} - \frac{\partial v}{\partial y} \frac{\partial \theta}{\partial y} - \frac{\partial w}{\partial y} \frac{\partial \theta}{\partial z} + \frac{\partial}{\partial y} \left(\frac{d\theta}{dt} \right) \end{aligned}$$

130 and
$$\frac{d\theta}{dt} = -\frac{\partial \overline{w'\theta'}}{\partial z}$$

131 we obtain

$$132 \quad \frac{d}{dt} \left(\frac{\partial \theta}{\partial y} \right) = -\frac{\partial u}{\partial y} \frac{\partial \theta}{\partial x} - \frac{\partial v}{\partial y} \frac{\partial \theta}{\partial y} - \frac{\partial w}{\partial y} \frac{\partial \theta}{\partial z} + \frac{\partial}{\partial y} \left(-\frac{\partial \overline{w'\theta'}}{\partial z} \right) \quad (3.2)$$

133 Here, u , v , and w denote the zonal, meridional, and vertical current velocity,
 134 respectively. Equation 3.2 describes the processes that act to generate/destroy the
 135 ocean front. The terms $-\frac{\partial u}{\partial y} \frac{\partial \theta}{\partial x}$, $-\frac{\partial v}{\partial y} \frac{\partial \theta}{\partial y}$, and $-\frac{\partial w}{\partial y} \frac{\partial \theta}{\partial z}$ are the contributions due to
 136 the mechanical processes: shear, convergence and tilting, respectively. The shear term
 137 represents conversion of the zonal temperature gradient into meridional gradient by

138 zonal current shear. In particular, the cool SST associated with the Benguela
 139 upwelling creates the strong zonal gradient in the south of the ABFZ (e.g., Morholz et
 140 al., 1999). The shear term can explain the conversion of such zonal gradient into
 141 meridional gradient. The convergence term represents strengthening/weakening of the
 142 meridional temperature gradient by convergence/divergence of meridional current.
 143 The tilting term represents conversion of the vertical stratification into meridional
 144 gradient by meridional shear of vertical velocity.

145 The fourth term is a thermodynamical term due to exchange of heat associated
 146 with the turbulent heat flux (surface heat flux is included into $w'\theta'$, it is the surface
 147 boundary condition). The contribution due to the second order horizontal diffusion is
 148 ignored for simplicity.

149 Since within the OML the temperature is fairly uniform (cf. Fig. 2 to compare
 150 the SST and OML-averaged temperature), we consider the OFGF with the mixed-
 151 layer mean quantities. With the approximation that temperature is independent of the
 152 depth in the OML (e.g., Kazmin and Rienecker, 1996; Tozuka and Cronin, 2014), Eq.
 153 3.2 can be expressed as,

154

$$155 \quad \frac{d}{dt} \left(\frac{\partial \theta_{oml}}{\partial y} \right) = - \frac{\partial u_{oml}}{\partial y} \frac{\partial \theta_{oml}}{\partial x} - \frac{\partial v_{oml}}{\partial y} \frac{\partial \theta_{oml}}{\partial y} - \frac{\partial (w_b + w_e)}{\partial y} \frac{\Delta \theta}{D} + \frac{\partial}{\partial y} \left(\frac{Q_s + Q_b}{\rho C_p D} \right) \quad (3.3),$$

156 where, the subscript of *oml* indicates the OML-mean quantity estimated by,

$$157 \quad A_{oml} = \frac{1}{D} \int_D^{surface} A \cdot dz$$

158 where, D denotes the OML depth, that is, the terms with subscription of oml include
 159 the changes in the OML implicitly. Although the horizontal velocity is a function of
 160 depth even in the OML, the horizontal mechanical terms in Eq. 3.3 can be written in
 161 terms of OML-mean quantities because the production remains linear relation as long
 162 as the temperature is independent of depth in the OML. w_b , w_e , $\Delta\theta$ and D represent
 163 the vertical velocity, the entrainment velocity, the temperature jump at the bottom of
 164 the OML, and the OML depth, respectively. According to Moissan and Niller (1998),
 165 the entrainment velocity at the bottom of the OML is estimated by

$$166 \quad w_e = \frac{\partial D}{\partial t} + \mathbf{u}_b \cdot \nabla D$$

167 here, \mathbf{u}_b is the horizontal velocity at the bottom of the OML. $\Delta\theta$ is estimated as the
 168 difference between the OML-mean temperature and the temperature at one-below
 169 layer of the OML. We use constant values for sea water density, ρ (1000 kg/m³) and
 170 isobaric specific heat of sea water, C_p (4200 Jkg⁻¹K⁻¹). The vertical mixing term is
 171 replaced with Q_s and Q_b , where $Q_s = (-\overline{w'\theta'})_{z=0}$ is the surface net heat flux at the
 172 top of OML (downward is positive in this study) and $Q_b = (-\overline{w'\theta'})_{z=D}$ represents
 173 the vertical mixing at the bottom of the OML, *i.e.*, in the thermocline. We assume that
 174 there is no penetration of shortwave radiation beyond the OML to deeper ocean
 175 layers. Because the vertical turbulent mixing term at the mixed-layer base Q_b is
 176 represented according to K-profile parameterization in OAGCMs; it will be not
 177 addressed explicitly in this study as it is not possible to estimate it from the reanalysis
 178 outputs.

179 While Eq. 3.3 is Lagrangian form of the OFGF, the equation can be also
 180 expressed in Eulerian form as below:

$$181 \quad \frac{\partial}{\partial t} \left(\frac{\partial \theta_{oml}}{\partial y} \right) = \underbrace{-\frac{\partial u_{oml}}{\partial y} \frac{\partial \theta_{oml}}{\partial x}}_{\text{SHER}} - \underbrace{\frac{\partial v_{oml}}{\partial y} \frac{\partial \theta_{oml}}{\partial y}}_{\text{CONF}} - \underbrace{\frac{\partial w_b}{\partial y} \frac{\Delta \theta}{D}}_{\text{TILT}} + \underbrace{\frac{\partial}{\partial y} \left(\frac{Q_s}{\rho C_p D} \right)}_{\text{SFLX}} + \underbrace{\text{residual}}_{\text{RESD}} \quad (3.4).$$

182 In this equation, we have some simplifications: the contribution due to the
 183 entrainment velocity at the bottom of the OML is included in RESD since its
 184 contribution is of higher order and it might be difficult to obtain an accurate
 185 estimation of the entrainment velocity from CFSR outputs. The contribution due to
 186 the vertical mixing Q_b , is estimated as residual of Eq. (3.4). Along with the vertical
 187 mixing, the residual term also includes the horizontal and vertical advection of the
 188 $\partial \theta_{oml} / \partial y$ which are not related to Lagrangian sources of the frontogenesis either. In
 189 the remainder of this paper, the shear term will be referred to as SHER, the
 190 confluence as CONF, the tilting as TILT, the thermodynamic term as SFLX and the
 191 residual as RESD.

192 Note that basically, our climatology is a 29-year mean from 1982 to 2010.
 193 However, some years do not have OML data at some grid points around the coastal
 194 region. For these grid points, we make the climatology only for available years. For
 195 example, the smallest number in the focusing ABFZ is 16 years at 16.25 °S.

196

197 **4. Overview of the ABFZ and its Seasonal Cycle in CFSR data**

198 Before the dynamical diagnosis is performed, we provide a brief overview of
 199 the main feature of the ABFZ. The maximum of the ABFZ (up to 1.4 °C/100km) is
 200 located at 16 °S just near the coast (Fig.1b). Figure 2a shows a seasonal cycle of the
 201 temperature and its meridional gradient obtained from the satellite product OISST. In
 202 this study, the maximum value of the meridional SST gradient is defined as the

203 **intensity of the ABFZ.** The core (SST meridional gradient exceeds 1.0 °C/100km) of
204 the ABFZ always lies between 17 °S and 15 °S. At **climatological** seasonal scale, the
205 location of the ABFZ exhibits rather weak variability compared to strong interannual
206 variability associated with the Benguela Niños that push the ABFZ southward due to
207 the southward intrusion of tropical warm water (e.g., Gammelsrød et al. 1998; Veitch
208 et al., 2006; Rouault et al., 2017). For instance, Rouault et al. (2017) showed that
209 during Benguela Niño 2010-2011 the ABFZ displaced southward as far as 20°S. The
210 intensity of the ABFZ shows a pronounced seasonal cycle: there are two peaks of the
211 strength in April-May and November-to-December, respectively. The semi-annual
212 cycle of the ABFZ will be examined in more details in the following sections. Figures
213 2b and c evidence that the CFSR reanalysis reproduces realistically the annual cycle
214 of the ABFZ, and that the annual cycle of the corresponding OML-mean temperature
215 meridional gradient is representative of the annual cycle of the SST meridional
216 gradient in terms of both timing and intensity of the two annual peaks. This latter
217 result justifies our approach to diagnose the frontogenesis of the ABFZ with the
218 OML-mean quantities.

219

220 **5. Diagnosis on **the frontogenesis of the ABFZ****

221 In this section, we investigate the frontogenesis of the ABFZ diagnostically
222 applying the OFGF described in Section 3. Figure 3 illustrates the climatological
223 annual-mean oceanic dynamical fields. The southwestward Angola and
224 northwestward Benguela alongshore currents collide just south of the ABFZ. Seaward
225 from the ABFZ, a strong westward current is detected. Intense upwelling (vertical
226 velocity at the bottom of OML exceeding 0.18 m/day) is generated along the coast in

227 the Benguela Current region. A local maximum of upwelling in the ABFZ
228 (approximately 17 °S) corresponds to one of the most vigorous upwelling cells in the
229 region, namely [Kunene upwelling](#) cell (Kay et al., 2018). Note also a relatively weak
230 downwelling cell (vertical velocity down to -0.06 m/day) just seaward from the Cape
231 Frio upwelling cell.

232

233 *5.1 Annual-mean state*

234 Figure 4 presents the annual-mean climatology of the 5 forcing/source terms
235 of the OFGF superimposing the meridional gradient of the OML-mean temperature.
236 SHER works frontolytically (destroying the front, about $-2\text{ }^{\circ}\text{C}/100\text{ km}\times 10^{-7}\text{ s}^{-1}$) in the
237 most parts of the ABFZ except just near the coast at 17 °S, although its frontogenetic
238 (generating front) contribution here is rather weak (less than $2\text{ }^{\circ}\text{C}/100\text{ km}\times 10^{-7}\text{ s}^{-1}$).
239 CONF has on average an intense frontogenetic contribution to the ABFZ (up to
240 $5\text{ }^{\circ}\text{C}/100\text{ km}\times 10^{-7}\text{ s}^{-1}$), especially offshore around 16 °S where the ABFZ is centered
241 (Fig. 2). The frontogenetic effect of CONF is consistent with GC2014 (the
242 frontogenesis of the SST front associated with the equatorial Atlantic cold tongue is
243 due to the confluence of northern South Equatorial Current and Guinea Current) and
244 can be expected because the warm and cold currents meet around the ABFZ. Note
245 however a small zone just near the coast at 16 °S where the CONF is frontolytic. This
246 local frontolytic contribution is overcompensated by a strong frontogenesis due to TILT
247 (more than $5\text{ }^{\circ}\text{C}/100\text{ km}\times 10^{-7}\text{ s}^{-1}$ on average in the ABFZ core). An elongated
248 frontogenetic zone associated with TILT is found along the Angolan coast from 17°S to
249 11°S and corresponds to the upwelling tongue observed in the Angola current region
250 (Fig.3). On the other hand, TILT is frontolytic off the ABFZ (at 17°S, 11°E) where the

251 downwelling is dominant as shown in Fig.3. The role of the upwelling in the ABFZ
 252 development will be analyzed in more details in the Section 6.2.

253 In addition to the mechanical terms, the thermodynamical components also
 254 show some influences on the ABFZ. SFLX works frontogenetically just near the coast
 255 at 16°S and frontolytically south and north from the core of the ABFZ, although its
 256 contribution is almost negligible compared to the mechanical contribution. [Annual-](#)
 257 [mean climatology](#) of RESD is estimated by,

$$258 \quad \text{RESD} = \frac{\partial u_{oml}}{\partial y} \frac{\partial \theta_{oml}}{\partial x} + \frac{\partial v_{oml}}{\partial y} \frac{\partial \theta_{oml}}{\partial y} + \frac{\partial w_b}{\partial y} \frac{\Delta \theta}{D} - \frac{\partial}{\partial y} \left(\frac{Q_s}{\rho C_p D} \right) \quad (5.1)$$

259 where, [the](#) local temporal tendency of the front, $(\partial \theta_{oml} / \partial y) / \partial t$ is [zero because the](#)
 260 [annual-mean climatology is independent of time. That is, the left-hand side of Eq.](#)
 261 [\(3.4\) is zero and RESD can be estimated. Note that all terms in Eq\(5.1\) is annual-](#)
 262 [mean climatology.](#) On average in the core of the ABFZ, RESD shows a strong
 263 frontolytic contribution around the core of the ABFZ (Fig. 4e). On the other hand,
 264 frontogenesis is located in the southern part of the ABFZ. This may be due to, at least,
 265 to vertical mixing at the base of the OML accounted for in RESD. According to
 266 GC2014, the turbulent mixing (surface and thermocline heat fluxes) is frontolytic in
 267 the equatorial front.

268

269 *5.2 Seasonal Cycle*

270 In the preceding subsection, we have shown that in terms of climatological
 271 annual-mean terms CONF and TILT of the OFGF are the main [sources](#) for the ABFZ
 272 generation. Next, we analyze the annual cycle of the ABFZ and its relationship to the

273 seasonal variations of the OFGF terms. As shown in Fig.2, the seasonal cycle of the
274 ABFZ exhibits two peaks. Note that if the seasonal cycle is sinusoidal, Eq. 3.4 implies
275 $\pi/2$ out of phase between the OFGF and temperature meridional gradient. This
276 means that for a semi-annual oscillation the temperature meridional gradient should
277 shift the OFGF by approximately 1 and half months.

278 Figure 5a illustrates the box-mean (10 °E-12 °E and 17 °S-15 °S) temporal
279 series of the meridional gradient of temperature obtained from satellite and reanalysis
280 products (the time series is smoothed by a 11-days-mean moving filter). This box
281 covers the maximum of the ABFZ in each month since the meridional location of the
282 ABFZ is almost stable in climatological seasonal cycle. There is an obvious semi-
283 annual cycle of the ABFZ with maxima in April-May and in November-December,
284 respectively, and minima in February-March and July-August, respectively (see also
285 Fig.2). The first maximum develops rapidly (during 2 month, from March to April)
286 whereas the development of the second maximum is somewhat slower (3 months,
287 from August to October). Figure 5a also evidences that CFSR reproduces realistically
288 the semi-annual cycle, although the magnitudes of the CFSR meridional SST gradient
289 are generally slightly stronger with respect to OISST. Corresponding to the annual
290 cycle of the ABFZ, there is a seasonal cycle of frontogenesis and frontolysis in Fig. 5a
291 as the tendency of the ABFZ (green line): two maxima in frontogenesis in March-
292 April and September-October and in frontolysis in May-June and December-
293 February. The tendency of the ABFZ is estimated by Equation of 5.2.

294 We further analyze the seasonal cycle of the OFGF terms. Similarly to the
295 climatological state in Fig. 4, the contributions of SHER and SFLX are relatively
296 small and do not seem to be responsible for either of the two peaks in the ABFZ
297 annual cycle (not shown). Figure 5b shows the seasonal variations of TILT, CONF,

298 and RESD averaged over the same box as the temperature gradients in Fig. 5a. For
 299 estimation of seasonal variation of RESD, the tendency of the meridional gradient is
 300 calculated as,

$$301 \quad \frac{\partial}{\partial t} \left(\frac{\partial \theta_{oml}(t)}{\partial y} \right) = \frac{\frac{\partial \theta_{oml}(t+1)}{\partial y} - \frac{\partial \theta_{oml}(t-1)}{\partial y}}{\Delta t}, \quad (5.2)$$

302 where, t and Δt denotes each time step and difference in time step, in this case, Δt is
 303 two days (2×86400 seconds). With this tendency at each day, RESD(t) is estimated by

$$304 \quad \text{RESD}(t) = \frac{\partial}{\partial t} \left(\frac{\partial \theta_{oml}(t)}{\partial y} \right) - \text{SHER}(t) - \text{CONF}(t) - \text{TILT}(t) - \text{SFLX}(t).$$

305 From the middle of November to February, the box-averaged CONF is
 306 modestly negative, which is due to the frontolytic effect adjacent to the Angolan coast
 307 as shown in Fig. 4b (however, CONF is frontogenetic off the ABFZ). The
 308 contribution of CONF becomes positive from March, although its frontogenetic
 309 contribution is relatively weak ($< 1.0 \text{ }^\circ\text{C}/100 \text{ km} \times 10^{-7} \text{ s}^{-1}$) until July. From the end of
 310 July CONF starts to increase and reaches its maximum ($3.0 \text{ }^\circ\text{C}/100 \text{ km} \times 10^{-7} \text{ s}^{-1}$) in the
 311 end of August. The frontogenetic contribution of CONF remains strong until the
 312 beginning of October but then rapidly decrease to become frontolytic in November.

313 The contribution of TILT to the ABFZ seasonal cycle is almost always
 314 frontogenetic. Close to zero in January, TILT is enhanced from February and reaches
 315 its maximum value ($3.0 \text{ }^\circ\text{C}/100 \text{ km} \times 10^{-7} \text{ s}^{-1}$) in March-April. In May-June, the
 316 frontogenetic effect of TILT gradually decreases (down to $1.0 \text{ }^\circ\text{C}/100 \text{ km} \times 10^{-7} \text{ s}^{-1}$) until
 317 December. The maxima in TILT and CONF correspond to the two periods of
 318 development of the ABFZ at seasonal scale: from March to April and from August to

319 October, respectively (Fig. 5a). This suggests that the two peaks of the ABFZ are
320 associated with two different mechanical terms and thus are due to two different
321 physical processes. On the other hand, the two periods of decay of the ABFZ are
322 consistent with the periods of weak frontogenetic and/or frontolytic contributions of
323 both TILT and CONF (as observed by Mohrholz et al., 1999), in December-February
324 and June-July, respectively.

325 In addition, RESD is almost always frontolytic with a relatively large
326 oscillation (0.0 to -5.0 $^{\circ}\text{C}/100$ $\text{km}\times 10^{-7}$ s^{-1}) as shown in Fig.5b. In particular, the
327 frontolytic effect due to RESD is stably strong (around -3.0 $^{\circ}\text{C}/100$ $\text{km}\times 10^{-7}$ s^{-1}) from
328 May to August when the ABFZ becomes weakened and frontogenetic effects due to
329 CONF and TILT are relatively weak (Figs. 5a and b). Conversely as TILT and CONF,
330 RESD does not exhibit a clear signal of semi-annual cycle, but rather an annual-cycle.
331 We thus can conclude that in terms of a first-order estimation, the semi-annual cycle
332 of the ABFZ is explained by the combination of TILT and CONF.

333

334 **6. Discussion**

335 The previous section showed that the two periods of development of the
336 ABFZ in March-April and August-October were due to a large extent to the
337 contribution of TILT and CONF, respectively. In this section, we investigate what
338 components are responsible for the corresponding peaks in TILT and CONF.

339

340 *6.1 Meridional Confluence*

341 CONF represents changes in the meridional temperature gradient associated
342 with ocean dynamics of convergence/divergence of meridional current, $\partial v_{oml} / \partial y$.
343 Figure 6a presents the annual cycle of $\partial v_{oml} / \partial y$ averaged over the ABFZ. In the
344 ABFZ, the meridional current is almost always convergent except for weak
345 divergence from November to January. The convergence of the meridional current is
346 maximum from August to mid-October (up to $-3.0 \times 10^{-7} \text{ s}^{-1}$) and is rapidly weakened
347 during November. The seasonal fluctuations in the convergence are associated with
348 changes in intensity and meridional extension of the southward Angola Current and
349 northward Benguela Current that meet in the ABFZ. Around the ABFZ, an area of
350 lower sea surface height (SSH) is formed, so-called Angola Dome, which shows a
351 pronounced seasonal cycle (e.g., Doi et al., 2007). Such well-organized SSH spatial
352 variability induces the geostrophic current, which can contribute to the current system
353 around the ABFZ. Therefore, here, we also focus on the SSH and corresponding
354 geostrophic current. Figure 6b illustrates the annual cycle of OML-mean meridional
355 current and meridional component of geostrophic current estimated from SSH at
356 15°S (north of the core of the ABFZ) and 17°S (south of the core of the ABFZ)
357 averaged between 10°E and 12°E . At 15°S the OML-mean meridional current is
358 southward all year round, except the beginning of May when a weak northward flow
359 is observed. The maximum southward meridional velocity occurs in October ($-$
360 0.12 m/s). At 17°S the OML-mean meridional current is northward in March-June and
361 shows a bi-annual peak of southward current in January-to-mid-February and October
362 indicating intrusion of tropical warm water to the ABFZ (e.g., Rouault, 2012). Figure
363 6b clearly evidences that the region between 17°S and 15°S is expected to be
364 convergent. The most convergent period is in September-October when the CONF
365 contribution to frontogenesis is the largest as shown in Fig. 5b. Another relatively

366 strong convergent period is from April to June when the meridional current is rather
367 northward at 17 °S and close to zero at 15° S. The period of weak
368 convergence/divergence, from December to February, corresponds to frontolytic
369 contribution of CONF (Figs.5b). Figure 6b evidences that the OML-mean meridional
370 current can be explained, to a large extent, by the geostrophic surface current. While
371 the large part of the meridional current and its seasonal cycle around the ABFZ is
372 explained by geostrophic current associated with the SSH to the northwest of the
373 ABFZ, there are some differences between v_{oml} and v_g . These differences are due to
374 the Ekman and ageostrophic currents.

375 The spatial distributions of the climatological monthly mean SSH and surface
376 geostrophic current in January, April, and September are shown in Figure 7. Two local
377 minima of SSH are observed: one along the coast in the Benguela system and one
378 west of the ABFZ (centered at 14 °S and 6 °E). The latter is associated with the
379 Angola Dome (e.g., Doi et al. 2007) and a strong cyclonic geostrophic flow reaching
380 the ABFZ. The geostrophic current generally generates the convergence in the ABFZ
381 (Fig. 6a). However, in January an intense divergence is generated due to the strong
382 southward ageostrophic current along the coast (Fig. 7a). In April, when CONF is
383 modestly frontogenetic (Fig.5b), the Angola Dome and associated geostrophic flow
384 are diminished (Fig. 7b) and a main source of convergence can thus be attributed to
385 the northward Benguela Current which penetrates into the ABFZ as far as up to 16 °S.
386 In September, whereas the low SSH sits in the south of the ABFZ as in April, the
387 Angola Dome is significantly developed to be related to a strong geostrophic current
388 resulting in a strong southward Angola Current intruding into the ABFZ along the
389 Angolan coast. The northward Benguela Current is relatively weak in September

390 compared to that in April. Thus, the maximum CONF in September is due to the
391 strong southward Angola Current.

392

393 *6.2 Tilting*

394 TILT is the second main contributor to generate the ABFZ especially in
395 March-to-May as shown in Figs. 4 and 5. In a first approximation TILT results from
396 the meridional gradient of vertical motion $\partial w_b / \partial y$ convoluted with the thermocline
397 stratification (e.g., Eq.3.4). Here, we explore more details of upwelling in the ABFZ.
398 The annual cycle of these two components averaged over the box [12 °E-10 °E] and
399 [17 °S-15 °S] (Fig.8) points out **the positive** $\partial w_b / \partial y$ and **the negative** stratification,
400 respectively, from January to August. This configuration leads to frontogenesis
401 through the TILT term (Fig. 5b). From August to December, $\partial w_b / \partial y$ changes sign
402 and the stratification becomes weaker; that explains why the TILT term is frontolytic
403 (especially in September) and its magnitude is weaker compared to January-August
404 because of a weaker stratification (**smaller vertical gradient in temperature**). Negative
405 $\partial w_b / \partial y$ can be seen in both March to April and August to September around the
406 ABFZ in Figs. S1a and b, but positive $\partial w_b / \partial y$ are also generated around the ABFZ
407 more in August-September than in March-April.

408 The OML depth has extrema in August to September (around 100 m) and from
409 January to April (around 20 m) indicating the seasonal cycle of solar insolation
410 forcing. Also the intensity of the thermocline shows a strong stratification from March
411 to May (2°C) and weak stratification from September to November (1.2°C). From
412 March to May TILT is the most dominant frontogenetic source because the OML is

413 the shallowest (20-30m), the stratification is the strongest (temperature jump in the
414 thermocline up to 2.0K) and the shear of vertical velocity $\partial w_b / \partial y$ is strongly
415 negative. The shallow OML and strong stratification can amplify the tilting effect due
416 to $\partial w_b / \partial y$. Conversely, TILT is weakly frontolytic from August to September when
417 the OML-depth is deepened (~100m), the stratification is weak (1.2K) and $\partial w_b / \partial y$ is
418 positive. Fig.S1c and d shows the differences in OML depth and ocean stratification
419 between March-April and August-September. Shallower OML and stronger
420 stratification can be seen everywhere around the ABFZ. Therefore, effects of both
421 positive and negative $\partial w_b / \partial y$ are reduced and consequently, contribution of TILT is
422 quite weak in August to September (Fig. 5b).

423

424 7. Concluding Remarks

425 In this study we investigated the processes controlling the ABFZ evolution
426 based on a first-order estimation of an ocean frontogenetic function (OFGF) applied
427 to the ocean mixing layer (OML) derived from the CFSR reanalysis. The OFGF
428 represents the temporal evolution of the meridional mixed-layer temperature gradient
429 and contains three mechanical terms (shear, convergence and tilting) and one
430 thermodynamical term. The residual term accounts for in particular vertical mixing at
431 the bottom of the OML (which is based on parameterization of turbulence *i.e.* highly
432 non-linear processes), entrainment velocity and horizontal/vertical advections of the
433 meridional temperature gradient. An analysis of the annual mean OFGF suggests that
434 the confluence effect (CONF) due to southward Angola Current (warm) and
435 northward Benguela Current (cold) is dominantly frontogenetic over the offshore part
436 of the ABFZ, although it has a local frontolytic effect just near the coast at 16°S. The

437 tilting effect (TILT) related to the coastal upwelling regime is another main
438 contributor to frontogenesis. Around the ABFZ, the intense Ekman transport
439 divergence is generated by wind stress curl (Fig. S2). This Ekman divergence induces
440 upward motion in the Ekman layer. Interestingly, the Ekman divergence due to the
441 zonal wind stress is also an important contributor to the vertical velocity in the ABFZ.
442 The contributions of the shear (SHER) and surface heat flux (SFLX) terms, are rather
443 negligible, while the residual (RESID) term represents a main frontolytic source.

444 Climatological seasonal evolution of the ABFZ has a well-pronounced semi-
445 annual cycle with two maxima of the SST meridional gradient, in April-May and
446 November-December, and two minima, in February-March and July-August. We
447 showed that the two maxima of the ABFZ were associated with two different
448 mechanical terms and due to two different physical processes. The development of the
449 first ABFZ maximum during March-April is mainly explained by the strong
450 contribution of TILT to frontogenesis, while the development of the second ABFZ
451 maximum during September-October is due to the frontogenetic contribution of
452 CONF. TILT is associated with the meridional gradient of the vertical velocity. The
453 annual maximum of TILT in March-April is due to a large extent to the combination
454 of the maximum stratification ($\Delta\theta$), shallow OML depth (D) and negative $\partial w_b / \partial y$
455 during this period. Indeed, in OFGF the ratio $\frac{\Delta\theta}{D}$ represents the efficiency by which
456 the meridional gradient of the coastal upwelling velocity can lead to the change of the
457 ABFZ intensity. Although the OML depth also modulates the surface heat flux
458 contribution to the OFGF, the thermodynamical term does not show any significant
459 impact on the development of the ABFZ maximum in March-April. On the other
460 hand, the importance of the OML depth for the thermodynamical term was suggested

461 for frontogenesis in a SST front associated with western boundary current (Tozuka
462 and Cronin, 2014; Tozuka et al., 2018). The annual maximum of CONF in
463 September-October is related to an intensified southward Angola current that seems to
464 be induced [approximately](#) by a cyclonic geostrophic flow associated with the
465 development of the Angola Dome (e.g., Doi et al., 2007). [However, the geostrophic
466 current is not completely consistent with the OML-mean current. The difference can
467 be attributed to the Ekman transport and ageostrophic component.](#) A relatively smaller
468 contribution of CONF to frontogenesis is also observed in April and is due to the
469 intrusion of the northward Benguela Current to the ABFZ during this period.

470 Most CGCMs fail to reproduce realistic SST field and ABFZ location [with
471 respect to climatology](#). Among other causes, this can be due to a poor representation
472 of regional climate variables in CGCMs, such as upwelling favorable wind, wind drop
473 off [and consequently near-coastal wind curl](#), alongshore stratification and OML depth
474 (e.g., Xu et al., 2014; Koseki et al., 2018; Goubanova et al., 2018), that impact
475 directly the two main frontogenesis terms, CONF and TILT. The OFGF proposed in
476 the present study can be thus an appropriate tool to diagnose the performance of
477 CGCMs in the ABFZ and more generally in frontal zones. This study shows that
478 diagnosis developed for mesoscale studies are valuable for climate studies and can
479 help to identify the origin of biases which affect OGCMs.

480 [Whereas the present study focused on the climatological state of the ABFZ
481 and its seasonal cycle, the intensity and the location of the ABZF exhibits a strong
482 inter-annual variability \(e.g., Mohrholz et al., 1999; Rouault et al., 2017\). The further
483 investigation on how the contributions of the OFGF are modified in the case of
484 Bengulea Niño/Niña would provide further insight on the dynamics of the South-](#)

485 Eastern Tropical Atlantic and sources of the CGCMs bias which have been suggested
486 to develop as inter-annual warm events (e.g., Xu et al., 2014).

487 Effects of the turbulent mixing and the effect due to the entrainment velocity
488 at the mixed-layer base on frontogenesis were accounted by the residual of the
489 frontogenetic function. An accurate quantification of these effects requires using
490 simulations of a higher resolution ocean model for which the output of the
491 temperature tendency due to those processes are available. According to Giordani and
492 Caniaux (2014), the vertical mixing is also large contributor to the frontogenesis.
493 However by destroying the balance between the mass and circulation fields, the
494 assimilation procedure induces spurious effects on the entrainment processes which
495 justifies that this process was included in the residual term RESD. These are the main
496 limitations of this study because diapycnal mixing is often an important term of the
497 oceanic upper-layers heat budget which is tightly coupled with vertical motions
498 (Giordani et al., 2013). A more comprehensive understanding of this term would be
499 valuable to estimate the performance of CGCMs in the ABFZ and more generally in
500 coastal upwelling zones.

501

502 **Acknowledgement**

503 We greatly appreciate two anonymous reviewers for their constructive and helpful
504 comments. Also, we would like to express our appreciation to Dr. Kunihiro Aoki in
505 the University of Tokyo for his constructive discussion in the beginning of stage of
506 this study. We also thank to Dr. Guy Caniaux in MÉTÉO-France for their helpful
507 discussions. We utilized the versions of 2012Rb of MATLAB software package
508 provided by The MathWorks, Inc., (<http://www.mathworks.com>) and Grid Analysis

509 and Display System (GrADS, <http://www.iges.org/grads/>) to compute each dataset
510 and create figures. The research leading to these results received funding from the EU
511 FP7/2007-2013 under grant agreement to no. 603521 (EU-PREFACE).

512

513

514 **Reference**

- 515 Auel, H., and Verheye, H. M.: Hypoxia tolerance in the copepod *Calanoides*
516 *carinatus* and the effect of an intermediate oxygen minimum layer on copepod
517 vertical distribution in the northern Benguela Current upwelling system and the
518 Angola-Benguela Front. *J. Exp. Mar. Bio. Eco.*, **352**, 234-243,
519 doi:10.1026/j.jembe.2007.07.020, 2007.
- 520 Chavez, F. P., and Messié, M.: A comparison of eastern boundary upwelling
521 ecosystem. *Prog. Oceanogr.*, **83** (1-4), 80-96 (Dec,
522 <http://www.sciencedirect.com/science/article/pii/S0079661109000998>, 2009.
- 523 Chelton, D.B., and Xie, S.-P.: Coupled ocean-atmosphere interaction at ocean
524 mesoscales. *Oceanography*, **23(4)**, 52-69, doi:10.5670/oceanog.2010.05, 2010
- 525 Chen, Z., Yan, X.-H., Jp, Y.-H., Jiang, L., and Jiang, Y.: A study of Benguela upwelling
526 system using different upwelling indices derived from remotely sensed data.
527 *Continental Shelf Research*, **45**, 27-33, 2012.
- 528 Colberg, F., and Reason, C. J. C.: A model study of the Angola Benguela Frontal

529 Zone: Sensitivity to atmospheric forcing. *Geophys. Res. Lett.*, **33**, L19608,
530 doi:10.1029/2006GL027463, 2006.

531 Colberg, F., and Reason, C. J. C.: A model investigation of internal variability in
532 the Angola Benguela Forntal Zone. *J. Geophys. Res.*, **112**, C07008,
533 doi:10.1029/2006JC003920, 2007.

534 Dinniman, M. S., and Rienecker, M. M.: Frontogenesis in the North Pacific Ocean
535 Frontal Zones-A Numerical Simulation. *J. Phy. Oceanogra.*, **29**, 537-559, 1999.

536 Doi, T., T. Tozuka, Sasaki, H., Masumoto, Y., and T. Yamagata, T.: Seasonal and
537 interannual variations of oceanic conditions in the Angola Dome.
538 *J. Phys. Oceanogr.*, **37**, 2698-2713, doi:10.1175/2007JPO3552.1, 2007.

539 Fennel, W., Junker, T., Schmidt, M., and Mohrholz, V.: Response of the Benguela
540 upwelling system to spatial variations in the wind stress. *Continental Shelf Research*,
541 **45**, 65-77, 2012.

542 Florenchie, P., Lutjeharms, J. E., Reason, C. J. C., Masson, S., and Rouault, M.:
543 The source of Benguela Ninos in the South Atlantic Ocean.
544 *Geophys. Res. Lett.*, **30**, doi:10.1029/2003GL017172, 2003.

545 Gammelsrød, T., Bartholomae, C. H., Boyer, D. C., Filipe, V. L. L., and O'Toole, M. J.:
546 Intrusion of warm surface water along the Angolan-Namibian coast in
547 February-March 1995: the 1995 Benguela Nino.
548 *South African Journal of Marine Science*,

549 **19:1**, 41-56, doi:10.2989/025776198784126719, 1998.

550 Giordani, H., and Caniaux, G.: Sensitivity of cyclogenesis to sea surface temperature in
551 the Northwestern Atlantic. *Mon. Wea. Rev.*, **129**(6), 1273-1295, 2001.

552 Giordani, H., and Caniaux, G.: Diagnosing vertical motion in the Equatorial Atlantic.
553 *Ocean Dynamics*, **61**(12), doi:10.1007/s10236-01—0467-7, 2012.

554 Giordani, H., Caniaux, G., and Voldoire, A.: Intraseasonal mixed-layer heat
555 budget in the equatorial Atlantic during the cold tongue development 2006.
556 *J. Geophys. Res.*, **118**, 650-671, doi:10.1029/2012JC008280, 2013.

557 Giordani, H., and Caniaux, G.: Lagrangian sources of frontogenesis in the equatorial
558 Atlantic front, *Clim. Dyn.*, doi:10.1007/s00382-014-2293-3, 2014.

559 Goubanova, K., Illig, S., Machu, E., Garcon, V., and Dewitte, B.: SST subseasonal
560 variability in the central Benguela upwelling system as inferred from satellite
561 observation (1999-2009). *J. Geophys. Res.*, **118**, 4092-4110,
562 doi:10.1002/jgrc.20287, 2013.

563 Goubanova, K., Sanchez.Gomez, E., Frauen, C., and Voldoire A.: Role of remote and
564 local wind stress forcing in the development of the warm SST errors in the
565 southeastern tropical Atlantic in a coupled high-resolution seasonal hindcast,
566 *Clim. Dyn.*, doi:10.1007/s00382-018-197-0, 2018.

567 Griffies, S. M., Harrison, M. J., Pacanowski, R. C., and Rosati, A.: Technical guide
568 to MOM4. GFDL Ocean Group Technical Report No.5, 337 pp. [Available online at

569 www.gfdl.noaa.gov/-fms], 2004.

570 Hansingo, K., and Reason, C. J. C.: Modelling the atmospheric response over southern
571 Africa to SST forcing in the southeast tropical Atlantic and southwest subtropical
572 Indian Oceans. *Int. J. Climatol.*, **29**, 1001-1012, doi:10.1002/joc.1919, 2009.

573 Hastenrath, S. and Lamb, P.: On the dynamics and climatology of surface flow over the
574 equatorial oceans. *Tellus*, **30**, 436-448, 1978.

575 Hirst, A. C., and Hastenrath, S.: Atmosphere-Ocean Mechanisms of Climate
576 Anomalies in the Angola-Tropical Atlantic Sector. *J. Phys. Oceanogr.*, **13**,
577 1146-1157, doi:http://dx.doi.org/10.1175/1520-
578 0485(1983)013<1146:AOMOCA>2.0.CO;2, 1983.

579 Junker, T., M. Schmidt, and Mohrholz, V.: The relation of wind stress curl and
580 meridional transport in the Benguela upwelling system. *J. Marine Res.*, **143**, 1-6,
581 2015

582 Junker, T., Mohrholz, V., Siegfried, L., and van der Plas, A.: Seasonal to interannual
583 variability of water mass characteristics and current on the Namibian shelf.
584 *J. Mar. Syst.*, **165**, 36-46, doi:10.1016/j.jmarsys.2016.09.003, 2017.

585 [Kay, E., Eggert, A., Flohr, A., Lahajnar N., Nausch, G., Nuemann, A., Rixen, T., Schmidt, M.,
586 Van der Pla, A., and Wasmund, N., 2018. Biogeochemical processes and turnover
587 rates in the Northern Benguela Upwelling System. *J. Mar. Syst.*, **188**, 63-80.](#)

588 Kazmin, A. S., and Rienecker, M. M.: Variability and forntogenesis in the large-scale

589 oceanic frontal zones. *J. Geophys. Res.*, **101**, 907-921, 1996.

590 Keyser, D., Reeder, M. J., and Reed, R. J.: A Generalization of Petterssens's
591 Frontogenesis Function and Its Relation to the Forcing of Vertical Motion.
592 *Mon. Wea. Rev.*, 116, 762-780, 1988.

593 Klein S. A., and Hartmann, D. L.: The Seasonal Cycle of Low Stratiform Clouds.
594 *J. Climate*, **6**, 1587-1606, 1993.

595 Koseki, S., Keenlyside, N., Demissie, T., Toniazzo, T., Counillon, F., Bethke, I., Ilicak, M.,
596 and Shen, M.-L.: Causes of the large warm SST bias in the Angola-Benguela Frontal
597 Zone in the Norwegian Earth System Model. *Clim. Dyn.*, **50**, 4651-4670,
598 doi:10.1007/s00382-017-3896-2, 2018.

599 Kopte, R, Brandt, P., Dengler, M., Tchupalanga, P. C. M., Macueria, M., and Ostrowski, M.
600 : The Angola Current: Flow and hydrographic characteristic as observed at 11°S.
601 *J. Geophys. Res. Oceans*, **122**, 1177-1189, doi:10.1002/2016JC012374, 2017.

602 Lutz, K., Jacobeit, J., and Rathmann, J.: Atlantic warm and cold water events and
603 impact on African west coast precipitation. *Int. J. Climatol.*, **35**, 128-141,
604 doi:10.1002/joc.3969, 2015.

605 Manhique, A.J., Reason, C. J. C., Silinto, B., Zucula, J., Raiva, I., Congolo, F., and
606 Mavume, A. F.: Extreme rainfall and floods in southern Africa in January 2013 and
607 associated circulation patterns. *Nat., Hazards*, **77**, 679-691, doi:10.1007/s11069-015-
608 1616-y, 2015.

609 Mohrholz, V., Schmidt, M., Lutjeharms, J. R. E., and John, H.-C.H.: Space-time
610 behavior of the Angola-Benguela Frontal Zone during the Benguela Niño of
611 April 1999. *Int. J. Remote Sensing*, **25**, 1337-1400,
612 doi:10.1080/01431160310001592265, 2004.

613 Patricola, C. M., and Chang, P.: Structure and dynamics of the Benguela low-level coast
614 jet. *Clim. Dyn.*, doi:10.1007/s00382-016-3479-7, 2016.

615 Pfeifroth, U., Hollmann, R., and Ahrens, B.: Cloud Cover Diurnal Cycles in Satellite
616 Data and Regional Climate Model Simulations.
617 *Meteorologische Zeitschrift*, **21**, 551-560, 2012.

618 Risien, C. M., and Chelton, D. B.: A global climatology of surface wind and wind stress
619 fields from 8 years of QuikSCAT scatterometer data. *J. Phy. Oceano.*, **38**, 2379-2413,
620 2008.

621 Rouault, M., Florenchie, P., Fauchereau, N., and Reason, C. J. C.: South east
622 tropical Atlantic warm events and southern African rainfall.
623 *Geophys. Res. Lett.*, **30**, 8009, doi:10.1029/2002GL014840, 2003.

624 Rouault, M.: Bi-annual intrusion of tropical water in the northern Benguela upwelling.
625 *Geo. Phys. Lett.*, **39**, L12606, doi:10.1029/2012GL052099, 2012.

626 Rouault, M., Illig, S., Lübbecke, J., and Koungue, R. A. I.: Origin, development and
627 demise of the 2010-2011 Benguela Niño. *J Mar. Syst.*,
628 <http://dx.doi.org/10.1016/j.jmarsys.2017.07.007>, 2017.

629 Saha S., and Co-authors.: The NCEP Climate Forecast System Reanalysis.
630 *Bull. Ame. Meteor. Soc.*, doi:10.1175/2010BAMS3001.1, 2010.

631 Santos, F., Gomez-Gesteria, M., deCastro, M., and Alvarez, I.: Differences in coastal and
632 oceanic SST trends due to the strengthening of coastal upwelling along the Benguela
633 current system. *Continental Shelf Research*, **34**, 79-86, 2012.

634 Small, R. J., Thomas, R. A., and Bryan, F. O.: Storm track response to Ocean Fronts in a
635 global high-resolution climate model. *Clim. Dyn.*, doi:10.1007/s00382-013-1980-9,
636 2014.

637 Stommel, H.: The Gulf Stream: a physical and dynamical description. 2nd ed. University
638 of California Press, Berkley and Cambridge University Press, London, 1965.

639 Tozuka, T., and Cronin, M. G.: Role of mixed layer depth in surface frontogenesis: The
640 Agulhas Return Current front. *Geophys. Res. Lett.*, doi:10.1002/2014GL059624,
641 2014

642 Tozuka, T., Ohishi, S., and Cronin, M. G.: A metric for surface heat flux effect on
643 horizontal sea surface temperature gradients. *Clim. Dyn.*, **51**, 547-561,
644 doi:10.1007/s00382-017-3940-2, 2018.

645 Veitch, J. A., Florenchie, P., and Shillington, F. A.: Seasonal and interannual
646 fluctuations of the Angola-Benguela Frontal Zone (ABFZ) using 4.5 km
647 resolution satellite imagery from 1982 to 1999. *Int. J. Remote Sensing*, **27**,
648 987-998, doi:10.1080/01431160500127914, 2006.

649 Vizzy, E. K., Cook, K. H., and Sun, X.: Decadal change of the south Atlantic ocean
 650 Angola-Benguela frontal zone since 1980. *Clim. Dyn.*,
 651 <https://doi.org/10.1007/s00382-018-4077-7>, 2018.
 652 Xu Z., Chang, P., Richter, I., Kim, W., and Tang, G.: Diagnosing southeast tropical
 653 Atlantic SST and ocean circulation biases in the CMIP5 ensemble. *Clim. Dyn.*, **43**,
 654 3123-3145, doi:10.1007/s00382-014-2247-9, 2014.

655

656 **Figures**

657

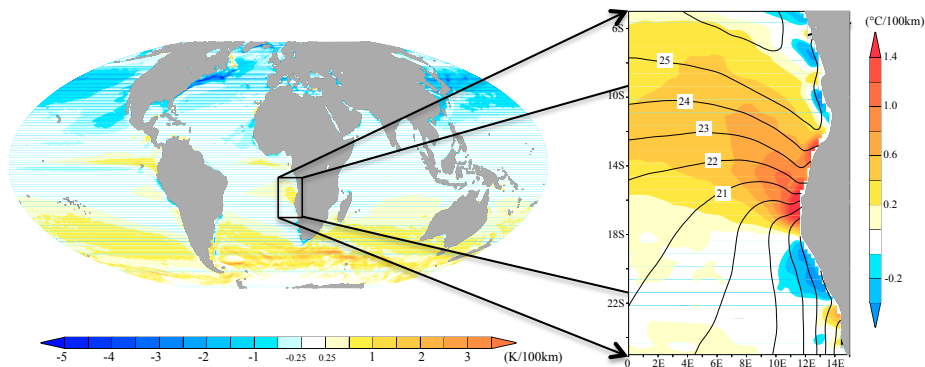


Figure 1.
 (Left) Global image of observed annual-mean SST meridional gradient from 1982-2010 of OISST. (Right) annual-mean SST (contour, °C) and its meridional gradient (°C/100km) around the ABFZ.

658

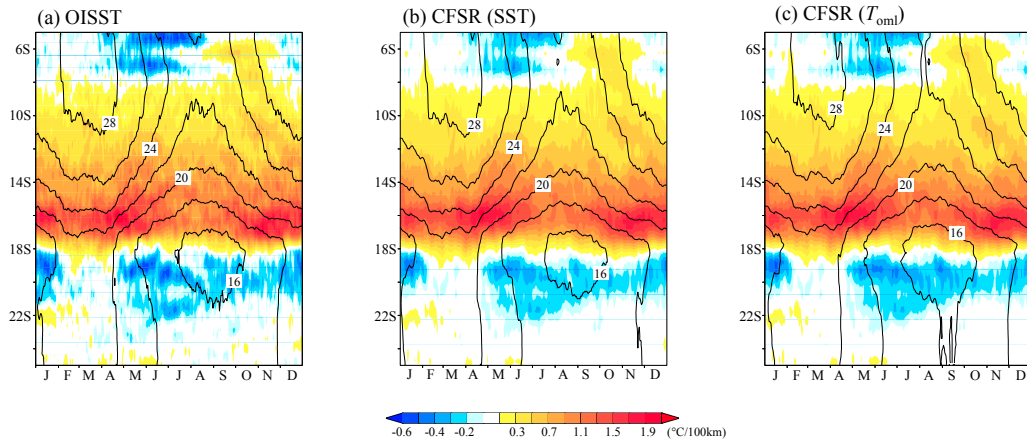


Figure 2. Climatological seasonal cycle of the temperature (contour) and its meridional gradient averaged between 10°E and 12°E for (a) SST of OISST, (b) SST of CFSR, and (c) OML-mean potential temperature of CFSR.

659

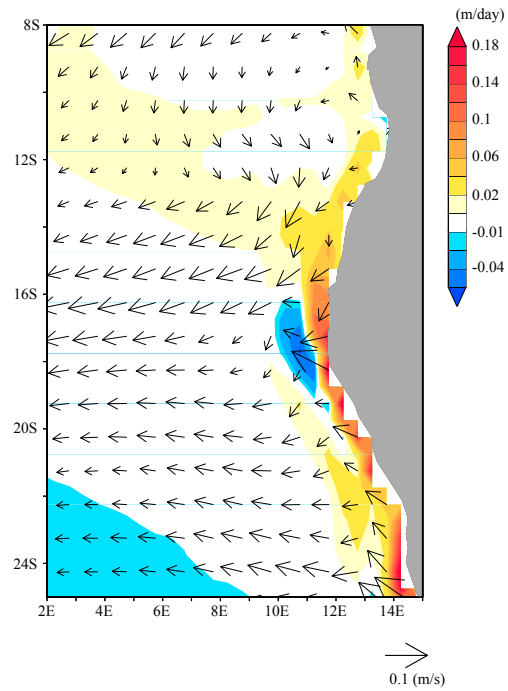


Figure 3. Annual-mean climatological states of OML-mean horizontal current (arrows) and vertical velocity at the bottom of OML (color).

660

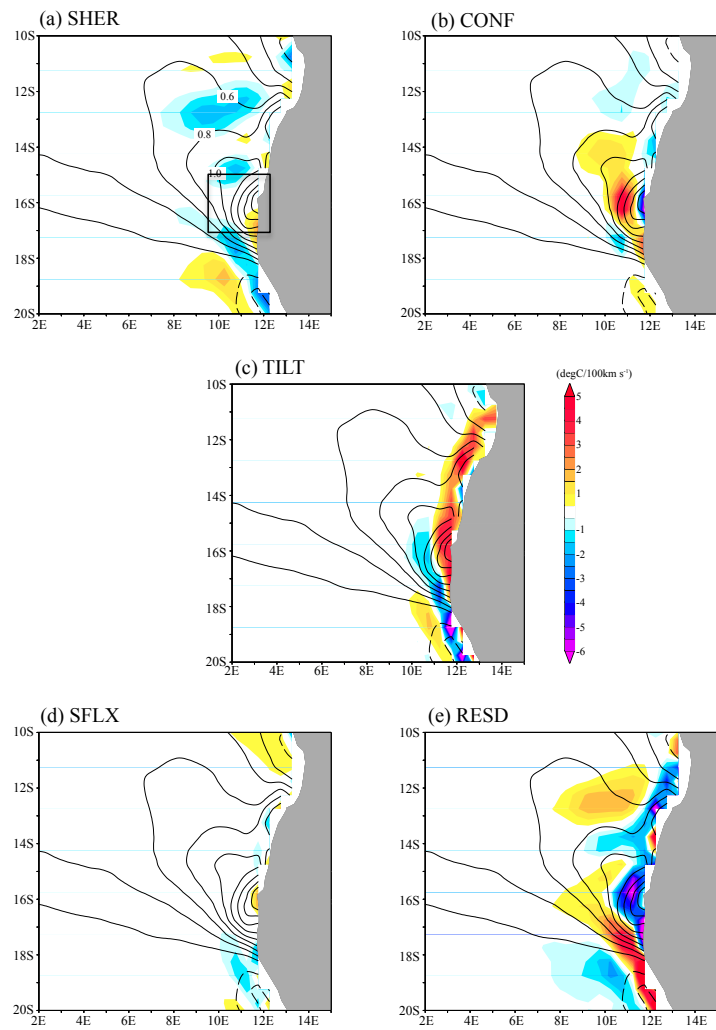


Figure 4. Annual-mean climatology of each term in OFGF. Contour is annual-mean climatology of meridional gradient of OML-mean potential temperature of CFSR ($^{\circ}\text{C}/100\text{km}$). The black box on (a) is the ABFZ used for the analysis in this study.

661

662

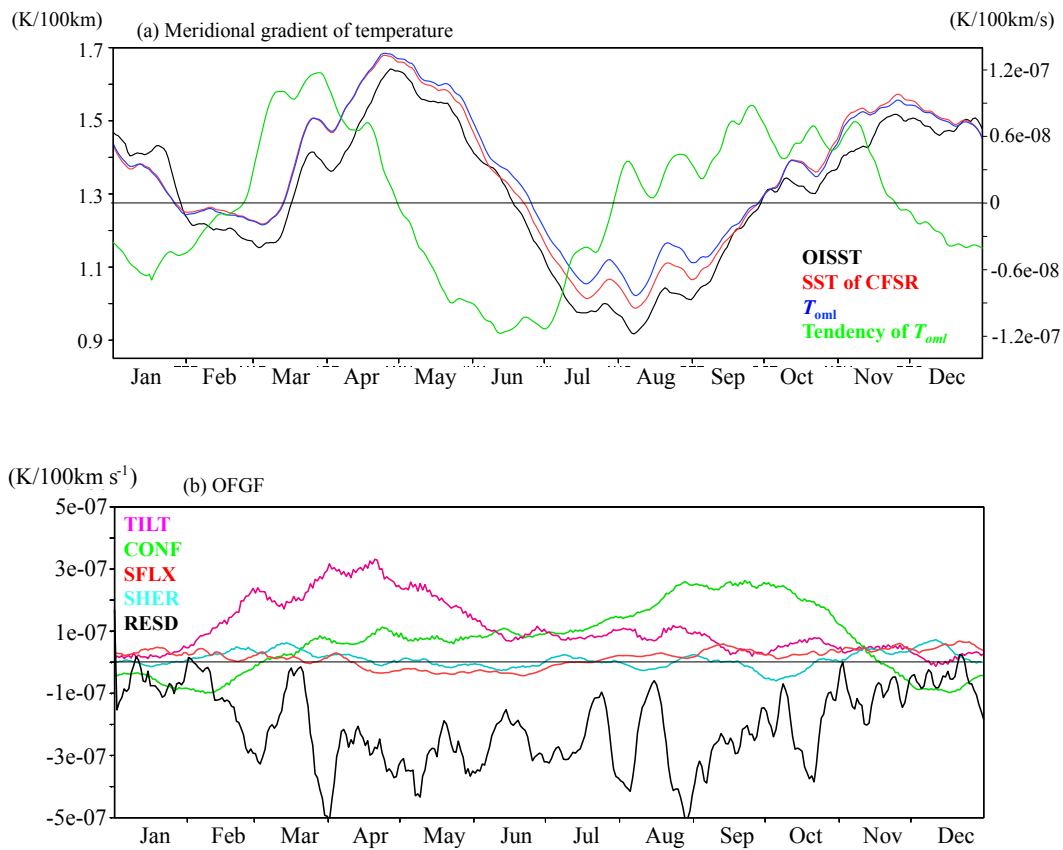


Figure 5. Box-mean (17°S-15°S and 10°E-12°E) time series of (a) meridional gradient of temperature (black: OISST, red: SST of CFSR, and blue: OML-temperature of CFSR) and (b) TILT (magenta), CONF (green), SHER (cyan), SFLX (red), and RESD (black). 11days-running mean are shown for all the time series.

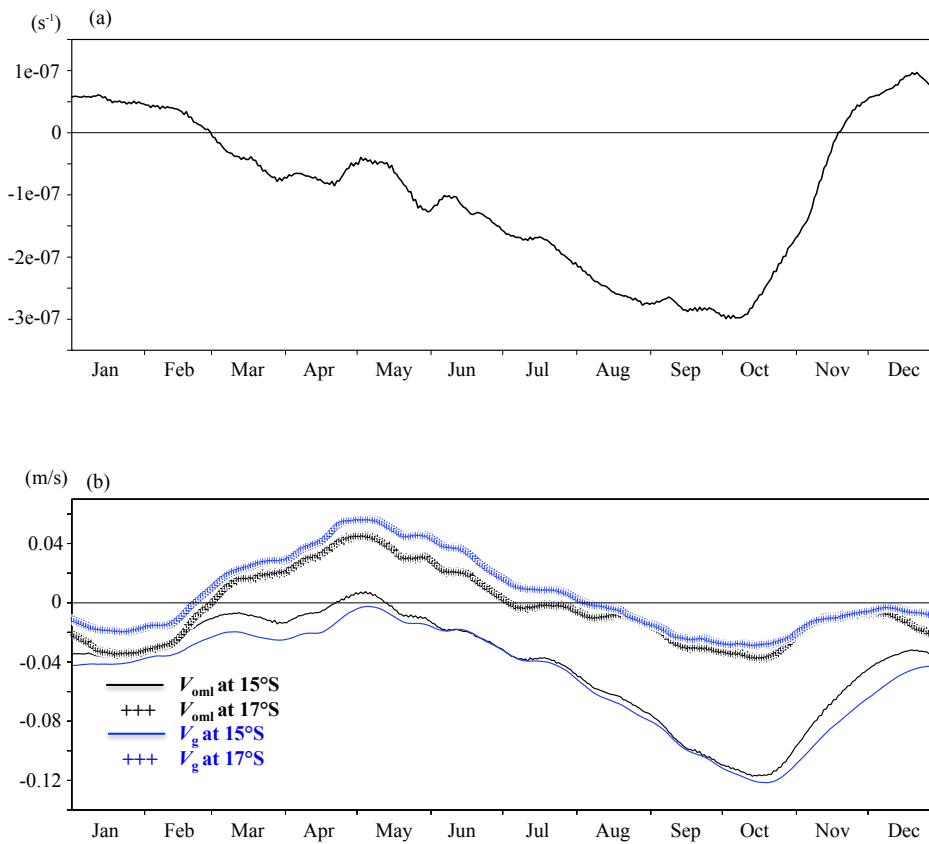


Figure 6. Time series of (a) $\partial v_{oml} / \partial y$ averaged over ($17^{\circ}S$ - $15^{\circ}S$ and $10^{\circ}E$ - $12^{\circ}E$) and (b) OML-mean meridional current velocity (black) and geostrophic meridional current velocity estimated from sea surface height (blue) at $15^{\circ}S$ (solid line) and $17^{\circ}S$ (+ mark) averaged between $10^{\circ}E$ and $12^{\circ}E$. All variables are filtered by moving 11-days window.

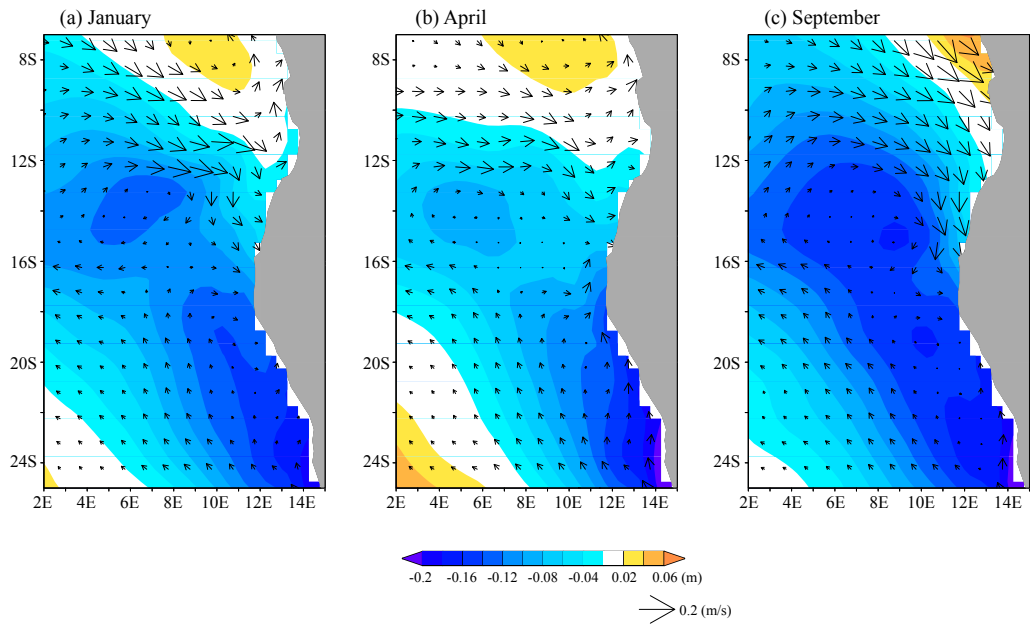


Figure 7. Monthly mean SSH (color) and geostrophic current (arrows) for (a) January, (b) April, and (c) September.

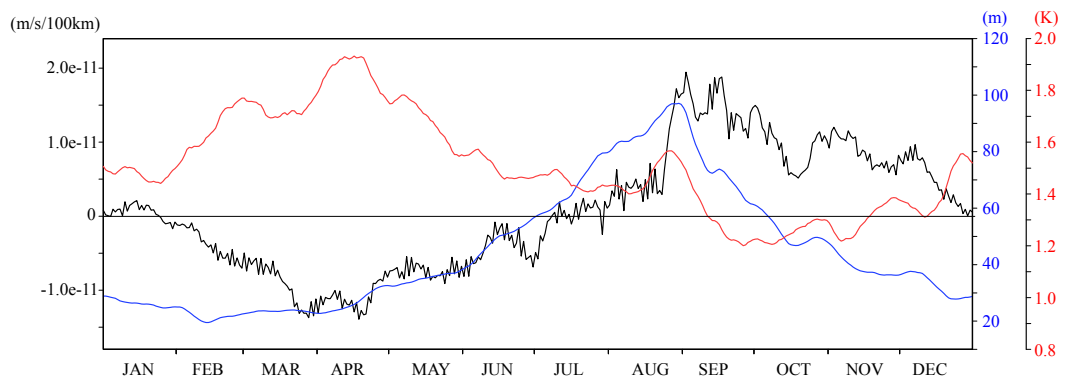


Figure 8. Time series of the area-averaged meridional gradient of the vertical velocity at the bottom of OML (black), OML depth (blue), intensity of upper ocean thermocline stratification (red) over 17°S-15°S and 10°E-12°E. All variables are filtered by moving 11-days window.

666

667